

accepted September 2, 1997

UV DIAGNOSTICS FOR THE EMISSION LINE GAS IN ACTIVE GALAXIES

MARK G. ALLEN¹, MICHAEL A. DOPITA¹, AND ZLATAN I. TSVETANOV²

ABSTRACT

Optical diagnostic diagrams are frequently ambiguous as a test of the photoionization or fast shock models of the narrow line regions of active galaxies. Here, we present a set of UV line ratio diagrams which can discriminate between pure shock and photoionization modes of excitation, and to some extent, also discriminate shocks with ionized precursors from photoionization. These diagrams use relatively bright emission lines and reddening insensitive ratios and provide a practical observational test for separating the excitation mechanisms of the narrow line regions of active galaxies. The most useful diagrams are those involving the various ionization stages of Carbon, ($[\text{O III}] \lambda 5007/\text{H}\beta$) *vs.* ($\text{C IV } \lambda 1549/\text{He II } \lambda 1640$) and the purely UV ratio pair ($\text{C II} \lambda 2326/\text{C III} \lambda 1909$) *vs.* ($\text{C IV } \lambda 1549/\text{C III} \lambda 1909$). Temperature sensitive FUV lines $\text{C III } \lambda 977$ and $\text{N III } \lambda 991$ also provide good discriminants. The models are compared to observations of nearby AGN, and also to high redshift objects where the UV lines are shifted into the optical.

Subject headings: galaxies:nuclei—galaxies:Seyfert—ultraviolet:galaxies

1. INTRODUCTION

Our knowledge of the energetics of Active Galactic Nuclei (AGN) is largely derived from observational interpretation of the effects of the nucleus on its environment. In particular, studies of the mechanisms responsible for the ionization of the “narrow line region” (NLR) are important for understanding both the way the nucleus releases its energy, and in deriving the physical parameters of the active nucleus itself.

¹Mount Stromlo and Siding Spring Observatories, The Australian National University, Private Bag Weston Creek P.O., ACT 2611, Australia; mga, mad@mso.mso.anu.edu.au

²Department of Physics and Astronomy, Johns Hopkins University, Baltimore MD 21218, USA; zlatan@pha.jhu.edu

Energetic processes occurring close to the central black hole of an active galaxy are thought to give rise to a powerful ionizing continuum. These processes may include emission from a hot accretion disk and/or synchrotron emission, and subsequent Comptonization of highly energetic electrons, all of which may result, to first approximation, in a power law spectrum of the UV and X-ray ionizing photons. A power-law spectrum of photons is also suggested by the shape of the UV continuum observed in many moderately high redshift quasars and by the extrapolation of the UV continuum to the X-ray region of the spectrum. In photoionization models of the NLR, the gas is considered to be illuminated by the ionizing radiation from the nucleus producing the observed emission line spectrum. This scenario appeals to the unified schemes for AGN in which the nuclear engine and the broad line region are surrounded by an optically thick torus (Antonucci & Miller 1985). Well defined bi-conical shaped extended narrow line regions (ENLR) observed in some Seyfert 2s (Pogge 1989; Tadhunter & Tsvetanov 1989; Wilson & Tsvetanov 1994; Simpson et al. 1997) have been quoted as supporting evidence for this picture, the bi-conical shape being the result of shadowing of ionizing radiation from the nucleus by an optically thick torus.

Shocks provide an alternative mechanism for the ionization of the NLR based on the input of mechanical energy. High velocity shocks generate a powerful local UV radiation field which can ionize the gas and emit a highly excited emission line spectrum like that observed in the NLR. There is little doubt that shocks exist in the NLR and are important (at least) in determining the phase structure of the gas and in generating the outflows observed in a number of Seyfert galaxies. For example, Colbert et al. (1996) find that 6 out of a sample of 22 edge on Seyfert galaxies show morphological and/or kinematic evidence for large scale outflows along the minor axis. Turbulence and instabilities in these flows must generate shocks. These may arise as either bow shocks at the working surface of a jet or outflow, cloud shocks around inhomogeneities caught up in the outflow region, or as wall shocks generated by the development of Kelvin-Helmholtz instabilities (Sutherland, Bicknell, & Dopita 1993) or else produced within hypersonic shearing entrainment regions (Dopita et al. 1997).

The relative importance of shocks compared with photoionization in determining the overall energetics of the NLR has not yet been established. An hypothesis advanced by Dopita & Sutherland (1995, 1996; hereafter DS95 and DS96 respectively) is that emission in the NLR may be entirely due to shocks. Further evidence to support this concept has been adduced by Bicknell, Dopita, & O’Dea (1997) in the case of powerful Gigahertz-peak spectrum (GPS), compact steep spectrum (CSS), and compact symmetric objects (CSO). Seyfert galaxies are however radio quiet, and equipartition arguments suggest that the pressure in the relativistic plasma is inadequate to drive high-velocity shocks in the interstellar medium (Wilson, Ward, & Haniff 1988). Nonetheless there is a clear correlation of optical and radio morphologies in Seyfert galaxies (Wilson & Tsvetanov 1994; Capetti et al. 1995, 1996). The apparent shortfall of energy (as traced by the radio synchrotron emission) in the radio lobes available to drive the optical emission via shocks, may be altered if mass entrainment into the relativistic jet maintains a large fraction of the energy of the jet in a thermal phase undetected at radio wavelengths as suggested by Bicknell, Dopita, & O’Dea

(1997).

Traditionally, attempts to distinguish between different excitation mechanisms have relied on observations of emission lines at optical wavelengths. For example H II regions, planetary nebulae and active galaxies can be distinguished from one another on the optical line ratio diagrams [N II] $\lambda 6583/\text{H}\alpha$ *vs.* [O III] $\lambda 5007/\text{H}\beta$ and of [O II] $\lambda 3727/[\text{O III}] \lambda 5007$ *vs.* [O III] $\lambda 5007/\text{H}\beta$, [N II] $\lambda 6583/\text{H}\alpha$ or [O I] $\lambda 6300/\text{H}\alpha$ as described by Baldwin, Phillips, & Terlevich (1981, hereafter BPT). This scheme was revised by Veilleux & Osterbrock (1987) avoiding the use of the reddening sensitive [O II] $\lambda 3727/[\text{O III}] \lambda 5007$ ratio and setting down functional criteria for the choice of line ratios for diagnostic purposes. In particular, ratios should be made up of strong lines that are easy to measure in typical spectra, blended lines should be avoided, and the wavelength separation between the two lines should be small as possible so the ratio is relatively insensitive to reddening correction and flux calibration. In addition one should avoid ratios of forbidden lines of different elements which lead to problems of abundance ratio dependence.

The physical basis for this classification scheme is that the size of the partially ionized zone in which the low ionization lines [N II] $\lambda 6583$, [S II] $\lambda\lambda 6717,31$ and [O I] $\lambda 6300$ preferentially arise, depends strongly on the nature of the object. This zone is quite extended in objects photoionized by a spectrum containing a large fraction of high energy photons (such as a power-law), but is very thin when photoionized by OB stars which emit few photons with energy above 4 Ryd.

These optical tests have been unable to provide conclusive discrimination between shocks and photoionization because both of these mechanisms can reproduce most of the observed optical line ratios (DS96 and references therein). However, the intensities of the UV lines are predicted to be much stronger in shocks than in simple photoionization models. This is because the UV collisionally excited lines such as C IV $\lambda 1549$, C III $\lambda 977$, N III $\lambda 991$ emit strongly at the high temperatures ($2 \times 10^4 - 10^5$ K) in the cooling zone behind high velocity (150–500 km s⁻¹) shocks compared to photoionized plasma in which these species are excited at a temperature of $\sim 10^4$ K. The large differences in the rates of collisional excitation of these UV lines therefore provides a potential means to discriminate between the models.

The high electron temperatures generated in shocks compared to photoionization, can also be used to provide discriminants between the models. Electron temperatures indicated by the [O III] $\lambda 4363/[\text{O III}] \lambda 5007$ ratio typically exceed the predictions of single zone photoionization models by several thousand degrees (Tadhunter, Robinson, & Morganti 1989). The common interpretation of this is that an extra local source of heating such as shocks is required. Indeed, DS95 have shown that shocks come closer to reproducing the observations of this ratio in AGN. However, [O III] $\lambda 4363$ is a weak line and flux measurements in the literature may be inaccurate due to poor subtraction of the stellar continuum.³ Also recent multi-zone photoionization models

³Storchi-Bergmann et al. (1996) have recently described an accurate procedure for stellar subtraction in the region of the [O III] $\lambda 4363$ and He II $\lambda 4686$ lines.

are able to produce higher temperatures so this diagnostic is rendered somewhat more ambiguous. DS95 suggest that the definitive test between the models may lie with more sensitive, temperature dependent line ratios such as C III] $\lambda 1909$ /C III $\lambda 977$ and N III] $\lambda 1750$ /N III $\lambda 991$.

In this paper we demonstrate with the aid of line ratio diagrams, how the UV lines (N III $\lambda 991$, N III] $\lambda 1750$, C III $\lambda 977$, C IV $\lambda 1549$, C III] $\lambda 1909$, C II] $\lambda 2326$, He II $\lambda 1640$) alone, and in combination with the optical line ratios [O III] $\lambda 5007$ /H β and [Ne V] $\lambda 3426$ /[Ne III] $\lambda 3869$ can be used to discriminate between current shock and photoionization models and therefore provide a useful observational test of the excitation mechanism. The models used are the shock models of DS96, a set of single zone photoionization models (ionization parameter U sequences) calculated with the same code as the shock models, and the recent $A_{M/I}$ sequence from Binette, Wilson, & Storchi-Bergman (1996, hereafter referred to as BWS96). We have chosen reddening insensitive ratios of relatively bright lines that are accessible with instruments such as the *HST* Faint Object Spectrograph (FOS) and the Space Telescope Imaging Spectrograph (STIS), so that these diagrams can be used as a practical observational tool to probe the physics of the NLR.

This paper is organized as follows: The various models used for comparison are described in section 2. Section 3 describes the utility of UV lines as diagnostics and the rationale for the selection of line ratios, followed by plots of the model grids on line ratio diagrams. We discuss the diagnostic capabilities of each of the diagrams, and also compare the model grids to a small set of observations, where both optical and UV line intensities have been measured. Also we consider diagnostics that are useful for high- z AGN where the UV lines have been shifted into the optical band.

2. THE MODELS

2.1. Photoionization

The simplest photoionization models one can construct for the NLR involve a planar slab of gas which is illuminated by a power-law ($F_\nu \propto \nu^\alpha$) spectrum of ionizing radiation. The intensity of the radiation is specified by the ionization parameter, U , defined as the ratio of the density of impinging photons to the outer number density of the cloud⁴. Typically sequences of models in which U varies over the range $10^{-4} - 10^{-1}$ are compared to NLR spectra. These models have been remarkably successful at reproducing most of the observed optical line ratios (Ferland & Osterbrock 1986, Veilleux & Osterbrock 1987, Robinson et al. (1987), Binette, Courvoisier, & Robinson 1988). The difficulties with single zone models have recently been reviewed by BWS96. Problems include a too low [O III] temperature and the weak UV lines compared to the observations. In order to produce strong UV lines, high electron temperatures and strong coronal lines, the emissivity

⁴ $U = \frac{1}{cn_H} \int_{\nu_0}^{\infty} \frac{F_\nu d\nu}{h\nu}$ where F_ν is the incident monochromatic ionizing flux, ν_0 the ionization potential of H, n_H the density at the front face of the illuminated gas, and c the speed of light.

of the optically thin zone which gives rise to the higher ionization lines, must be raised relative to the optically thick zone. This can be done in composite models which include both optically thick (ionization bounded) clouds and optically thin (matter bounded) clouds, by increasing the solid angle subtended by the optically thin clouds relative to the optically thick clouds. In this fashion, BWS96 combine matter bounded (MB) and ionization bounded (IB) components so that the MB component absorbs $\sim 40\%$ of the ionizing spectrum, corresponding to the exhaustion of He^+ ionizing photons and the peak in the effective heating rate in the cloud. The IB component is illuminated by the ionizing continuum that has been filtered by the MB component. The MB component is responsible for most of the He II emission, and the ionization bounded component emits low to intermediate excitation lines. Previous multi-component models considered smooth distributions of cloud sizes (Morganti et al. 1991) and combinations of thin MB clouds with IB clouds (Viegas & Prieto 1992). In BWS96 IB and MB components are combined into a sequence parameterized by $A_{M/I}$, the solid angle ratio of MB clouds relative to IB clouds.

In computing the photoionization models we have used the multi-purpose MAPPINGS II code. This is the same code as was used for the DS96 shock models, and is most recently described in Sutherland, Bicknell, & Dopita (1993). The same solar abundance set as used by DS96 was used for photoionization models. This gives the advantage of removing abundance and atomic data differences and facilitates a direct comparison between shock and photoionization models. We compute a set of U sequences using a power-law ionizing source input spectrum ($F_\nu \propto \nu^\alpha$) with spectral indices $\alpha = -1, -1.4$. A high energy cutoff of 100 Ryd (1.36 keV) was chosen so as to avoid over predicting the intensity of the soft X-rays with such flat spectral indices. The range in ionization parameter was $10^{-4} < U < 1$, and density $100 < n < 1000 \text{ cm}^{-3}$. The models were ionization bounded with a matter filling factor of unity, and correspond to a range in cloud sizes 0.003–32 pc.

The line ratios for the $A_{M/I}$ sequence are derived from the line intensities for MB and IB components given by BWS96. Table (2) in BWS96 gives the intensities for the MB and IB components for the single case of an $\alpha = -1.3$, $U_{MB} = 0.04$, power-law continuum incident on the MB clouds, and the IB clouds illuminated by the continuum that is filtered by the MB clouds. These parameters were chosen by BWS96 so as to give an optimum description of Seyfert and LINER spectra. Line ratios for a given $A_{M/I}$ were calculated according to the prescription given by equation (2) in BWS96. We consider the range $0.001 < A_{M/I} < 100$ which encompasses the range used in the BWS96 ($0.04 < A_{M/I} < 16$). A larger value of $A_{M/I}$ gives a larger weight to the MB component, and therefore a higher excitation spectrum. Also, as discussed in BWS96, $A_{M/I}$ cannot strictly be less than unity because the MB clouds are by definition intervening between the IB clouds and the ionizing source. An apparent $A_{M/I} < 1$ may however be observed if some of the MB clouds are obscured along the line of sight. Variations on this sequence are clearly possible, for instance by varying U_{MB} , α , or the thickness of the MB component. However the $A_{M/I}$ sequence used in this paper is the only such sequence currently available in the literature and further investigation of the potential of this approach is beyond the scope of this paper.

2.2. Shock models

Shocks have been incorporated into models of the NLR in various ways. In the simplest picture shocks serve to compress the gas which is then illuminated by a central ionizing source (Pedlar, Dyson, & Unger 1985; Taylor, Dyson, & Axon 1992). This situation is then modelled with simple photoionization codes. Viegas-Aldrovandi & Contini (1989) considered composite shock and photoionization models for clouds flowing either into, or away from, the nucleus. Models for which the shock itself generates enough ionizing radiation to form an equilibrium H II region in the precursor gas, called photoionizing shocks⁵ have been presented by DS96 form the basis for the shock comparisons discussed in this paper. DS95 present the line ratios predicted by these models, for a wide range of input shock parameters, as grids on optical line ratio diagnostic diagrams. They suggest that this mechanism may be solely responsible for the ionization of the NLR.

The physics of photoionizing shocks is described in detail in DS96. Their simplified, 1-d steady-flow, radiative shock models show that a fast radiative shock generates a strong local radiation field of ionizing photons in the high temperature, radiative zone behind the shock front. The dominant emission processes here are electron thermal bremsstrahlung and line emission. This radiation field is isotropic, and affects the ionization and thermal balance of the gas both ahead of, and behind, the shock front. Photons diffusing upstream may form an extensive precursor H II region. Photons diffusing downstream influence the ionization and temperature structure of the recombination zone of the shock. Transverse magnetic fields also play an important role by contributing to the pressure in the post-shock gas thereby limiting the compression factor of the shock. The collisionally excited UV lines are predominantly produced in the hot cooling zone of the shock close to the recombination region ($10^5 > T_e(\text{K}) > 10^4$). The hotter post-shock region ($T_e \sim 10^6$ K) is the source of the harder ionizing radiation generated in the shock.

The shock model grids have been calculated in the low density limit⁶, and are parameterized by the shock velocity V_{shock} , and the magnetic parameter B/\sqrt{n} . The shock velocity controls the shape of the ionizing spectrum produced by the shock, and the magnetic parameter controls the effective ionization parameter in the optically emitting recombination zone of the shock. The output line spectra from these models are available as part of the AAS CD-ROM Series, Vol. 7 (Leitherer et al. 1996). DS96 give scaling relations for the total bolometric, and $H\beta$ luminosities emitted by a shock, and show via optical line ratio diagrams that the output spectra from the shock models are similar to AGN spectra.

In section 3 we plot the DS96 model grids for combinations of these UV and optical lines. Both shock+precursor, and shock-only grids are included. The range in shock velocity is $150 < V_{shock} <$

⁵The name “autoionizing shocks” used by some authors is avoided because of the confusion with the atomic process of autoionization that has a separate meaning

⁶Densities $n_e < 1000 \text{ cm}^{-3}$ in the photo-absorption zone, corresponding to $n_e \lesssim 10$ for the preshock density. This ensures that lines used for diagnostic purposes are not seriously affected by collisional de-excitation.

500 km s⁻¹ for the shock only grids and $200 < V_{shock} < 500$ km s⁻¹ for the shock+precursor grids. The range of magnetic parameter is $0 < B/\sqrt{n} < 4 \mu\text{G cm}^{3/2}$. Values of $B/\sqrt{n} \sim 2 - 4 \mu\text{G cm}^{3/2}$ correspond to equipartition of the thermal and magnetic pressures in the pre-shock plasma. The intensity of He II $\lambda 1640$ is not given in the DS96 models, so we take the He II $\lambda 1640$ line flux to be 9 times the flux of He II $\lambda 4686$.

2.3. Limitations of the models

The most serious limitation of the shock models is the assumption of a steady one-dimensional flow. Secondary shocks which may occur in a proper three-dimensional treatment would affect the predictions of the lower ionization species most strongly. Another assumption is that the radiative transfer is treated in the downstream-only approximation. The transfer of the resonance lines, such as Ly α and C IV $\lambda 1549$, is treated according to a simple escape probability formulation for the local slab.

Resonance line transfer is, of course, highly sensitive to geometrical factors. In a planar shock the optical depth for resonance scattering will be highest in the compressed gas along the direction perpendicular to the shock front, so that the resonance line photons will be scattered preferentially into the upstream and downstream regions. The resonance line emission from the shock is then expected to be dependent on viewing angle in the sense that a shock viewed side-on will have lower relative flux of resonance lines.

Geometrical considerations are also important for photoionized gas. Villar-Martin, Binette, & Fosbury (1996) have considered the effects of resonance scattering and dust on the UV line spectrum of radio galaxies. Ly α is the most affected line, because it is subject to resonance scattering with very high optical depth both inside and outside of the ionized region, and is also absorbed by dust in regions of neutral material. We do not use Ly α in any of our diagnostics because these complications destroy any predictive capacity of this line. The effect on C IV $\lambda 1549$ is not as severe because the regions for resonance scattering of this line are limited to zones where C³⁺ exists, and in any case the line optical depths are far smaller than the case of Ly α .

3. DIAGNOSTIC DIAGRAMS

3.1. Utility of UV diagnostics

As described in the introduction, it is difficult to discriminate between fast shocks and photoionization by a hard photon spectrum, with the standard optical diagnostic diagrams. In shocks faster than 200 km s⁻¹, the photoionized precursor dominates the emission of many lines in the spectrum. Furthermore because the ionizing radiation responsible for the precursor has a substantial component of EUV photons it generates optical spectra which are not unlike those produced by

a power-law with an upper cutoff in frequency. Lower velocity shocks, or shocks without precursors (which have been the main type of shock models reported in the literature) generate optical line ratios which are almost indistinguishable from power-law photoionization with a very low ionization parameter ($U < 10^{-3}$).

A number of authors have searched for specific line ratios which are able to separate shocks and photoionization. Diaz, Pagel, & Wilson (1985) and Kirhakos & Phillips (1989) discussed the use of the ratio [S II] $\lambda\lambda 6717,31$ to the near infrared lines [S III] $\lambda\lambda 9069,9532$ to distinguish between shock and photoionization mechanisms in LINERs, while Osterbrock, Tran, & Veilleux (1992) considered other near infrared lines. Kirhakos & Phillips (1989) found that the shock models of Binette, Dopita, & Tuohy (1984) were separated from the power-law photoionization models of Stasinska (1984) on the [S II] $\lambda\lambda 6717,31/H\alpha$ *vs.* [S III] $\lambda\lambda 9069,9532/H\alpha$ diagram, and on other diagrams which employ the [S II] $\lambda\lambda 6717,31/[S III] \lambda\lambda 9069,9532$ ratio. Kirhakos & Phillips (1989) found also that the observed line ratios of AGN fell in between the two sets of models, so a clear distinction of the excitation mechanisms was not possible in this case. In that data set the LINERs showed the most scatter with respect to the models, while the Seyferts were more tightly grouped and fell closer to the photoionization models but still had too low [S III] $\lambda\lambda 9069,9532$ compared to the models.

DS96 present their shock models on a set of diagnostic diagrams, along with a database of Seyfert and LINER spectra. They found that Seyferts lie closer to predictions of shocks with precursors, while LINERs have line ratios predicted by shocks without precursors although there is significant scatter of the observations around the model grids. The ambiguity of determining the excitation mechanism from these lines arises because photoionization models have a considerable amount of overlap with both the shock and shock+precursor grids. DS96 emphasize the use of ultraviolet emission lines as better discriminants between shocks and photoionization because the UV resonance lines (eg. C IV $\lambda 1549$) which are predominantly produced in the cooling zone of the shock are predicted to be much stronger than in photoionization models that give the same optical spectrum.

Since the predictions of particular UV line ratios differ significantly between shock and photoionization models, it is possible to construct UV, and UV-optical line ratio diagrams in which the model grids are separated. In order to make these diagrams a practical tool for discriminating between the models we adopt criteria similar to Veilleux & Osterbrock (1987). We select lines which are relatively bright in active galaxies, and where possible use ratios of lines that are relatively close in wavelength to minimise the sensitivity to reddening corrections.

The line ratios we find most useful for comparing observations with the models are the UV line ratios C IV $\lambda 1549/He II \lambda 1640$, C IV $\lambda 1549/C III] \lambda 1909$, C II] $\lambda 2326/C III] \lambda 1909$, the near UV lines [Ne V] $\lambda 3426/[Ne III] \lambda 3869$. The ratios involving FUV lines N III] $\lambda 1750/N III \lambda 991$ and C III] $\lambda 1909/C III \lambda 977$, while not close in wavelength are included as a temperature sensitive diagnostic. In constructing line ratio diagrams we find that it is useful to combine these ratios

with the optical ratio $[\text{O III}] \lambda 5007/\text{H}\beta$, in order to better separate the various model grids. The diagnostic diagrams are presented in Figures 2 and 3 and we discuss each diagram individually in section 3.3. We also compare the new diagrams with one of the standard optical line ratio diagrams $[\text{O III}] \lambda 5007/\text{H}\beta$ *vs.* $[\text{N II}] \lambda 6583/\text{H}\alpha$.

For high redshift objects the UV lines are shifted into the optical band and the rest wavelength optical lines are less accessible, being in the near infrared. For these objects it is more useful to have diagnostics that rely only on UV lines. Villar-Martin, Tadhunter, & Clark (1997; hereafter VTC97) have recently used line ratio diagrams involving $\text{C IV } \lambda 1549/\text{He II } \lambda 1640$, $\text{C III] } \lambda 1909/\text{He II } \lambda 1640$ and $\text{C IV } \lambda 1549/\text{C III] } \lambda 1909$ to compare a database of 21 high- z radio galaxy spectra ($z > 1.7$), with various models including the shock models from DS96. On these diagrams the line ratios for the precursor gas have been plotted separately, rather than having the shock and precursor spectra summed to form a shock+precursor grid. Since the precursor gas is not resolved from the shocked gas it is inappropriate to compare such data with the precursor-only line ratios as the emission from the shock will also contribute to the observed spectrum. In section 3.5 we repeat the diagrams used by VTC97, with the shock-only, and shock+precursor grids appropriately combined.

3.2. Comparison with the observations

It is not the purpose of this paper to present a large data base of observations for comparison with the models. Instead, for most of our diagrams which use UV and optical lines, we confine the observational data to a small sample of objects for most of which we have obtained long wavelength baseline spectra with the *HST* FOS and ground based telescopes. We also include combined IUE, and HUT data on NGC 1068 collected from the literature. Since the diagnostics presented below rely on ratios of both optical and UV lines, we emphasize the need for wide wavelength coverage spectra to obtain as many of these diagnostic lines as possible.

For high- z objects the observational material has only UV coverage so we are obliged to use diagrams involving UV lines alone. However, the average high- z spectrum given by McCarthy (1993) has a wider spectral coverage, and can therefore be included in most diagrams.

Spectra of the NLRs in the Seyfert 2 galaxies NGC 5643 and NGC 5728 have been obtained with the FOS using the $0''.86$ square aperture. Both NGC 5643 and NGC 5728 have striking ionization cones seen in HST narrow band images (Wilson et al. 1993; Simpson et al. 1997) and show evidence for hidden nuclei. The aperture for the observations was located over the bright apex of the cone in each case. The high resolution FOS spectra covered the wavelength range $1150 - 2500 \text{ \AA}$, and observations with the FOS prism covering $1150 - 5400 \text{ \AA}$ allowed us to tie the flux scale to ground based optical observations. Ground based spectra were taken with the ANU 2.3 m telescope at Siding Spring with wavelength coverage $3000 - 10000 \text{ \AA}$. The details of the FOS spectra and the procedure used for joining the FOS and ground based spectra will be presented in a future paper.

The FOS spectrum of the central disk in M87 was taken with the $0''.86$ circular aperture positioned $0''.6$ from the nucleus, avoiding contamination of the emission line spectrum by continuum from the nucleus. The wavelength coverage is $1150 - 7000 \text{ \AA}$ and the spectrum reveals LINER-like line ratios. A full line list is given in Dopita et al. (1997) along with a detailed study of the central disk.

The line ratios for NGC 5643, NGC 5728 have been corrected for reddening assuming an intrinsic $H\alpha/H\beta$ ratio of 3.1, and using the reddening function of Cardelli, Clayton, & Mathis (1989). The corresponding visual extinctions for our NGC 5643 and NGC 5728 spectra are $A_V = 1.08$, and $A_V = 1.26$ respectively. The reddening for the M87 spectrum is taken to be $A_V=0.124$ (Dopita et al. 1997).

For NGC 1068, the very well studied Seyfert 2 galaxy, we have used the collated line flux measurements drawn from the literature by Dopita (1997). This is the only object for which we have measurements of the FUV lines N III $\lambda 991$ and C III $\lambda 977$, these come from the Hopkins Ultraviolet Telescope (HUT; Kriss et al. 1992).

The database of high- z radio galaxies is taken directly from Table 1 in VTC97. This consists of C IV $\lambda 1549$ /C III] $\lambda 1909$, C IV $\lambda 1549$ /He II $\lambda 1640$ and C III] $\lambda 1909$ /He II $\lambda 1640$ measurements for 21 radio galaxies with $z > 1.7$, mostly from van Ojik (1995), plus single objects from Elston et al. (1994), McCarthy et al. (1990), and Spinrad et al. (1985).

3.3. UV diagnostic diagrams

In all the diagrams presented below the shock-only, shock+precursor, and photoionization model grids are plotted with consistent line type and grid spacing. The shock-only grids are plotted in grey, and are labelled with magnetic parameter $B/\sqrt{n}= 0, 1, 2, 4 \mu\text{G cm}^{3/2}$, and shock velocity $V_{shock} = 150, 200, 300, 500 \text{ km s}^{-1}$. The shock+precursor grids are labelled with $V_{shock} = 200, 300, 500 \text{ km s}^{-1}$, and magnetic parameter where possible. The $\alpha = -1$ and the $\alpha = -1.4$ power-law photoionization U sequences are plotted for $n = 100 \text{ cm}^{-3}$ and $n = 1000 \text{ cm}^{-3}$ with grid lines of constant U every 0.25 dex. The $A_{M/I}$ sequence is labelled with $A_{M/I}$ over the range $0.001 \leq A_{M/I} \leq 100$, and tick-marks at intervals of 0.2 dex.

The reddening corrected data points for M87, NGC 1068, NGC 5643 and NGC 5728 are plotted as solid circles with their error bars, and the object names are indicated next to the points. Where possible we have included a data point (star) for the average high redshift radio galaxy of McCarthy (1993).

All diagrams include a reddening vector which indicates the effect of an extinction of $10 A_V$. Note that due to the 2175 \AA bump in the extinction law, the line ratio C IV $\lambda 1549$ /C III] $\lambda 1909$ decreases rather than increases with extinction.

Figure 1, $[\text{O III}] \lambda 5007/H\beta$ vs. $[\text{N II}] \lambda 6583/H\alpha$, is one of the standard optical diagnostic

diagrams. It is included here for comparison with the UV and UV-optical diagrams. The shape of the shock and shock+precursor grids on this diagram have been discussed by DS95 where the models are compared with a database of Seyfert and LINER spectra. DS95 finds that LINER spectra are closer to the shock-only grid while the Seyferts have spectra closer to the shock+precursor predictions. Power law photoionization models can also generate spectra in the same region of the diagram as the shock-only and shock+precursor model grids. In Figure 1 the high velocity part of the shock-only grid coincides with the power-law photoionization sequences for $U \sim 10^{-3.5}$, and the high velocity end of the shock+precursor grid overlaps the higher $U \sim 10^{-2.5}$ photoionization models. In the following optical-UV and UV diagnostic diagrams we demonstrate that the pure shocks can be cleanly separated from the photoionization, and that $V_{shock} < 400 \text{ km s}^{-1}$ shocks with precursors can be discriminated from photoionization.

3.3.1. ($[O \text{ III}] \lambda 5007/H\beta$) vs. ($C \text{ IV } \lambda 1549/He \text{ II } \lambda 1640$) and ($C \text{ IV } \lambda 1549/C \text{ III] } \lambda 1909$)

In Figures 2a and 2b we combine the commonly used $[O \text{ III}] \lambda 5007/H\beta$ ratio with the UV ratios $C \text{ IV } \lambda 1549/He \text{ II } \lambda 1640$, and $C \text{ IV } \lambda 1549/C \text{ III] } \lambda 1909$. The UV ratios have been chosen with the criteria discussed above, and specifically to include $C \text{ IV } \lambda 1549$ because of the large differences in the shock and photoionization model predictions for the strength of this line. We note that $C \text{ IV } \lambda 1549/He \text{ II } \lambda 1640$ utilizes $He \text{ II } \lambda 1640$ as a recombination line reference in the UV, much as $H\beta$ is used in the optical. The $C \text{ IV } \lambda 1549/C \text{ III] } \lambda 1909$ ratio has the additional advantage of being independent of abundance.

In shocks, the $He \text{ II } \lambda 1640$ line flux relative to the Balmer lines increases monotonically with shock velocity (DS95) and $C \text{ IV } \lambda 1549$ is always strong as a result of collisional excitation. In contrast, photoionization models generate similar $He \text{ II } \lambda 1640$ flux for a given spectral index since this line arises from recombination, and the $C \text{ IV } \lambda 1549$ line intensity is determined primarily by the temperature structure of the H II region, being generally stronger as the ionization parameter increases.

It is useful to combine the UV line ratios $C \text{ IV } \lambda 1549/He \text{ II } \lambda 1640$ and $C \text{ IV } \lambda 1549/C \text{ III] } \lambda 1909$ with the optical ratio $[O \text{ III}] \lambda 5007/H\beta$ since this ratio separates the two types of shock models. Simple shock models without photoionized precursors have lower $[O \text{ III}] \lambda 5007/H\beta$ than shock+precursor models because the $[O \text{ III}] \lambda 5007$ emission is dominated by the precursor zone. The ionization state of the precursor gas is a strong function of shock velocity, so in the shock+precursor case, $[O \text{ III}] \lambda 5007/H\beta$ increases monotonically with shock velocity, from 1.5 at $V_{shock} = 200 \text{ km s}^{-1}$ to 12.6 at $V_{shock} = 500 \text{ km s}^{-1}$. The dependence on shock velocity arises because higher velocity shocks produce a harder spectrum of ionizing photons, which increases the temperature and effective ionization parameter in the precursor zone. Under these conditions $[O \text{ III}] \lambda 5007$ becomes relatively more efficient as a coolant, with the effect of increasing $[O \text{ III}] \lambda 5007/H\beta$. Figures 2a and 2b show the separation of shock+precursor, and shock-only grids along the $[O \text{ III}] \lambda 5007/H\beta$ axis. The two grids begin to merge for low velocity shocks where the precursor emission is negligible, and the line

ratios are dominated by the shock rather than by the precursor.

Figures 2a and 2b confirm that C IV $\lambda 1549$ /He II $\lambda 1640$ and C IV $\lambda 1549$ /C III] $\lambda 1909$ are strong functions of U in the power-law photoionization models. For example C IV $\lambda 1549$ /He II $\lambda 1640$ increases from $10^{-4.5}$ at $U = 10^{-4}$, to approximately 1.6 at $U = 0.1$. The photoionization model grids show that in order to produce the C IV $\lambda 1549$ /He II $\lambda 1640$ ratio as strong as predicted by the shock models (0.4–16), a relatively high ionization parameter $U \gtrsim 0.01$ is required. The ionization parameter required to reproduce the UV line strengths observed in AGN is generally higher than that indicated by the observed optical lines (cf. Figure 1). Power-law photoionization models for Seyferts typically require ionization parameters $U = 10^{-3}$ to 10^{-2} ($\alpha \sim -1.5$) to reproduce the optical line ratios (Ho, Shields, & Filippenko 1993). LINERs, however, have low excitation optical spectra, with [O III] $\lambda 5007$ /H $\beta \lesssim 3$. Photoionization models for LINERs typically adopt a similar ionizing continuum to that used for Seyferts, $\alpha \sim -1.5$, but require a much lower ionization parameter ($U \sim 10^{-3.5}$) to reproduce the optical line ratios (Ho, Filippenko, & Sargent 1993). This can be seen in Figure 1, where the Seyferts NGC 1068, NGC 5643 and NGC 5728 indicate $U \sim 10^{-2.5} - 10^{-2.8}$ with respect to the photoionization models. The single zone, low ionization parameter photoionization models are however, unable to account for the strong UV lines and the C IV $\lambda 1549$ /He II $\lambda 1640$ ratio observed in some LINERs, such as M87. This is because, when the ionization parameter is low enough to produce a LINER-like spectrum in the optical, the electron temperature is too low to give appreciable excitation of the C IV $\lambda 1549$ line, or any other line in the far-UV.

Multiple-component photoionization models go some way to solve the problems of single zone models. The two component models of BWS96 which combine a MB component and an IB component, are able to produce relatively strong UV lines in combination with a low excitation optical spectrum. The $A_{M/I}$ sequence shown in Figure 2a has values of C IV $\lambda 1549$ /He II $\lambda 1640$ in the same range as the shock models. For values of $0.001 < A_{M/I} < 0.05$ the sequence is dominated by the IB component, with only a small fraction of MB clouds. Over this range of $A_{M/I}$ the [O III] $\lambda 5007$ /H β ratio remains relatively low at approximately 3.5. This value is comparable to the value of [O III] $\lambda 5007$ /H β predicted by power-law models with $U < 0.001$, although the input ionizing spectrum incident on the MB clouds has $U_{MB}=0.04$.

It is important to note that, while low values of $A_{M/I}$ correspond to a lower proportion of MB clouds, and a higher proportion of IB clouds, the line ratios calculated for the low $A_{M/I}$ end of the sequence do not generally converge to the values produced by the ionization bounded U sequence of the same ionization parameter. This is because the ionizing continuum which illuminates the IB component of the $A_{M/I}$ sequence is still filtered by the MB component even for low values of $A_{M/I}$, and is not therefore the same as the power law continuum used in the U sequences. As was mentioned in section 2.1, values of $A_{M/I}$ less than unity must correspond to an apparent $A_{M/I}$, in which the MB clouds are obscured from direct viewing along the line of sight.

When the ionization parameter for the photoionization models exceeds ~ 0.1 the ionization

structure of the cloud changes so that ionization balance for Carbon shifts to higher ionization stages, decreasing the emission of C IV $\lambda 1549$ relative to He II $\lambda 1640$. This effect causes the photoionization U sequence curves to reach a maximum in C IV $\lambda 1549$ /He II $\lambda 1640$ at 3.2 for the $\alpha = -1$ models and 1.6 for the $\alpha = -1.4$ models. The U sequences then fold over themselves at the high U end of the sequence, so that for some regions in Figure 1 there is a double valued photoionization solution. The diagnostic capability of this region of the diagram is limited by this effect which prevents the photoionization parameters from being uniquely determined, but the diagnostic capability is more seriously undermined by the fact that the photoionization models overlap with shock+precursor models with high magnetic parameter, and shock velocities in excess of 400 km s^{-1} . The reason for the overlap is that the ionizing radiation produced by a fast shock is not unlike a power-law distribution, so produces similar spectra to the high U photoionization models.

In the photoionization models the ratio C IV $\lambda 1549$ /C III] $\lambda 1909$ behaves in a similar way to the C IV $\lambda 1549$ /He II $\lambda 1640$ ratio for values of the ionization parameter $U \lesssim 0.1$. For higher values of U , the C IV $\lambda 1549$ /C III] $\lambda 1909$ ratio continues to increase whereas the C IV $\lambda 1549$ /He II $\lambda 1640$ ratio reaches a maximum. The photoionization grids in Figure 2 overlap with the high shock velocity ($V_{shock} > 400 \text{ km s}^{-1}$), shock+precursor grids, showing that photoionization models can produce values of the C IV $\lambda 1549$ /C III] $\lambda 1909$ ratio which lie in the same range as shocks, but in order to do so, a high ionization parameter is required. The $A_{M/I}$ sequence in Figure 2 has values of C IV $\lambda 1549$ /C III] $\lambda 1909$ in the range predicted by shocks for values of $A_{M/I} > 0.1$. Below this value, the C IV $\lambda 1549$ /C III] $\lambda 1909$ ratio decreases rapidly with $A_{M/I}$.

Comparing our set of observations to the model grids in Figure 2a, we find that the NLRs of the Seyfert 2 galaxies NGC 1068, NGC 5643, and NGC 5728 have line ratios which fall in a region where the shock+precursor grid, the high U end of the power-law photoionization U sequences, and the $A_{M/I}$ sequence all overlap. This obviously prevents us from unambiguously separating the emission mechanisms with these particular line ratios.

M87 has a LINER-like optical spectrum, and its low [O III] $\lambda 5007$ /H β ratio clearly separates it from the Seyferts in our diagrams. In both Figures 2a and 2b, M87 falls closest to the shock-only grid, with shock velocities between 200 and 300 km s^{-1} , and high magnetic parameter. This is a good example of the power of the UV diagnostics over the optical diagrams. For example, in Figure 1 objects with LINER like spectra such as M87 lie close to both shock-only and $U \sim 10^{-3.5}$ photoionization models, whereas Figures 2a and 2b which include UV lines, cleanly separate photoionization and shock-only grids which allows us to identify the M87 spectrum as shock excited. Single zone photoionization models for M87 have been explored by Dopita et al. (1997), where power-law, blackbody, and Bremsstrahlung continua have all been tuned to reproduce the observed [O III] $\lambda 5007$ /H β ratio. None of these cases can reproduce the UV lines which were predicted to be much weaker than observed. Furthermore, by using the shock grid as a starting point, Dopita et al. (1997) have calculated an optimized shock model for M87 giving a self-consistent shock velocity of 265 km s^{-1} , and magnetic parameter $B/\sqrt{n} = 5.4 \mu\text{G cm}^{3/2}$.

3.3.2. ($[O\ III] \lambda 5007/H\beta$) vs. ($[Ne\ V] \lambda 3426/[Ne\ III] \lambda 3869$)

$[Ne\ V] \lambda 3426$ is another high ionization line which, like $C\ IV\ \lambda 1549$, is always strong in shocks whilst being strongly dependent on ionization parameter in power-law photoionization models. We utilize the ratio of $[Ne\ V] \lambda 3426$ to $[Ne\ III] \lambda 3869$, these lines are close in wavelength, and the ratio is abundance independent. The shapes of the photoionization and shock model grids in Figure 2c are quite similar to Figures 2a and 2b. Like $C\ IV\ \lambda 1549/He\ II\ \lambda 1640$ in Figure 2a, $[Ne\ V] \lambda 3426/[Ne\ III] \lambda 3869$ reaches a maximum in the photoionization models near $U = 0.1$, but in contrast to Figures 2a and 2b, the $A_{M/I}$ sequence produces the highest excitation values of $[Ne\ V] \lambda 3426/[Ne\ III] \lambda 3869$.

On this diagram, Figure 2c, the Seyferts NGC 5728 and NGC 5643 fall within the $\alpha = -1.4$ power-law models, in the region where the grids fold back on themselves. Although this overlap prevents an accurate determination of the ionization parameter with these ratios, the points indicate ionization parameters in the range 0.03–0.3. NGC 1068 falls just outside the photoionization grids closer to the $A_{M/I}$ sequence. Compared to the shock+precursor models the Seyfert observations indicate an $[Ne\ V] \lambda 3426/[Ne\ III] \lambda 3869$ ratio approximately 0.5 dex higher than the shock+precursor grid. The M87 point is again consistent with the shock-only models, falling in the same location with respect to the grid as in Figure 2b.

A practical advantage of using $[Ne\ V] \lambda 3426$ and $[Ne\ III] \lambda 3869$ with $[O\ III] \lambda 5007$ and $H\beta$ is that these lines are accessible with ground based instruments for low redshift objects.

3.3.3. ($C\ II] \lambda 2326/C\ III] \lambda 1909$) vs. ($C\ IV\ \lambda 1549/C\ III] \lambda 1909$)

We find that the combination of the line ratio pairs $C\ II] \lambda 2326/C\ III] \lambda 1909$ and $C\ IV\ \lambda 1549/C\ III] \lambda 1909$, Figure 2d, are able to separate the photoionization model grids from the shock-only grid, and are also able to separate the shock+precursor grid from the photoionization grids to a greater extent than the previous diagrams. In this respect we regard this to be an important UV diagnostic for discriminating between the two competing mechanisms. Also, since the ratios involve only lines of different ionization stages of Carbon it is also insensitive to abundance effects.

In order to provide a unique discriminant between models on line ratio diagrams, model grids must not overlap. While there is formally no overlap between the shock+precursor grid and the photoionization U sequences, the $B/\sqrt{n} = 0\ \mu\text{G cm}^{3/2}$, $V_{shock} = 500\ \text{km s}^{-1}$ corner of the shock+precursor grid does approach very close to the $\alpha = -1\ U$ sequences. Note however that the $B/\sqrt{n} = 4\ \mu\text{G cm}^{3/2}$, $V_{shock} = 500\ \text{km s}^{-1}$ region of the shock+precursor grid, which overlaps the $\alpha = -1.4$ photoionization models in Figures 2a, 2b and 2c is separated from the photoionization models in Figure 2d. The $A_{M/I}$ sequence crosses the U sequences at both the low and high end of the $A_{M/I}$ parameter values, but otherwise has a distinct locus. Also, part of the $A_{M/I}$ sequence overlaps with the high velocity end of the shock+precursor grid, as it does in Figures 2a and 2b.

The NGC 1068 data point falls at the same position with respect to the shock+precursor grid in Figure 2d, as it did in Figures 2a and 2b, indicating that the $B/\sqrt{n} = 4 \mu\text{G cm}^{3/2}$, $V_{shock} = 480 \text{ km s}^{-1}$ shock+precursor model correctly reproduces the observed C II] $\lambda 2326$, C III] $\lambda 1909$, C IV $\lambda 1549$, He II $\lambda 1640$, [O III] $\lambda 5007$ and $H\beta$ fluxes for NGC 1068. The NGC 5643 and NGC 5728 points in Figure 2d fall inbetween the shock+precursor grid and the $\alpha = -1$ photoionization grids, making it difficult to assign either mechanism as dominant. NGC 1068 falls close to the $A_{M/I}$ sequence for $A_{M/I} \sim 0.5$, which is lower than indicated in Figures 2a, 2b and 2c, where the sequence indicates $A_{M/I} > 1$.

Because the shock-only model grids are well separated from the photoionization grids with the line ratios used in Figure 2 the C II] $\lambda 2326$ /C III] $\lambda 1909$ *vs.* C IV $\lambda 1549$ /C III] $\lambda 1909$ diagram constitutes a powerful diagnostic for discriminating between shock and photoionization mechanisms for LINER-like spectra. We find that M87 is a good example of this, whereby the optical line ratios can be equally well produced by photoionization or shocks, but that the UV ratios enable us to state unequivocally that this object is shock-excited. Consistent with all the previous diagrams, the M87 point falls on the shock-only grid with a shock velocity of $\sim 300 \text{ km s}^{-1}$ and high magnetic parameter.

As described above, the apertures used in the UV observations of the Seyferts encompassed the bright apex of the ionization cones near the inferred position of the hidden nucleus. It is not yet known how the UV line ratios vary spatially over the extent of the NLRs in these objects. The optical line ratios of these objects are known to vary throughout the NLR, and in some cases are suggestive of shock excitation. Spatially resolved UV spectroscopy of the NLRs of AGN will shed much more light on the relative importance of photoionization and shocks.

3.4. Temperature sensitive diagnostics

The temperature sensitive ratios such as N III] $\lambda 1750$ /N III $\lambda 991$, and C III] $\lambda 1909$ / C III $\lambda 977$ are potentially very useful for discriminating between shocks and photoionization. In shock models the FUV lines N III] $\lambda 1750$, and C III $\lambda 977$ are generated almost entirely within the shock structure, where the temperatures are much higher than possible in any photoionization model. In Figures 3a and 3b these ratios are combined with the optical ratio [O III] $\lambda 5007$ / $H\beta$. As in Figures 2a, 2b and 2c the [O III] $\lambda 5007$ / $H\beta$ ratio serves to separate the shock-only and shock+precursor grids.

In Figures 3a and 3b both types of shock model are completely separated from the photoionization models making this a very good diagnostic for discriminating between the models. Temperatures indicated by the N III] $\lambda 1750$ /N III $\lambda 991$, and C III] $\lambda 1909$ /C III $\lambda 977$ ratios are plotted along the top axis of the diagrams in intervals of 5000K up to 100000K. These temperature axes were calculated assuming purely collisional excitation in the low density limit ($n_e < 10^5 \text{ cm}^{-3}$) and using the collision strengths of Dufton et al (1978) for the C III ratio and Blum and Pradhan (1992) for the N III ratio. The observations of NGC 1068 derived from HUT and IUE spectra

indicate high temperatures; 47900 K from the N III] $\lambda 1750$ /N III $\lambda 991$ ratio and 26700 K from the C III] $\lambda 1909$ /C III $\lambda 977$ ratio. The line ratios predicted by the shock models are indicative of temperatures from 25000 K to >100000 K.

The $A_{M/I}$ sequences shown in Figures 3a and 3b were calculated in the same manner as all the previous diagrams, with MB and IB components for the C III $\lambda 977$ and N III $\lambda 991$ lines provided by Binette (private communication). N III $\lambda 991$ and C III $\lambda 977$ may be underestimated in the $A_{M/I}$ sequences as those calculations (done with MAPPINGS Ic) did not consider the effects discussed by Ferguson, Ferland, & Pradhan (1995).

The NGC 1068 observation indicates a temperature higher than possible with either the power-law photoionization or the $A_{M/I}$ sequence. It is more consistent with shocks in Figure 3a but falls inbetween the shock and photoionization model grids in Figure 3b.

3.5. High- z diagnostics

Here we consider the UV diagnostics which were used by VTC97 to investigate the balance between shocks and photoionization in high- z radio galaxies. They compare spectra of 21 high- z radio galaxies ($z > 1.7$) with photoionization models, and the shock models from DS96 using similar UV diagnostic diagrams to those presented in this paper. In their models they explore the effect of viewing angle on the spectrum of photoionized clouds. They consider clouds where the illuminated face is viewed directly, and the case where clouds are viewed from the rear. They find that $\alpha = -1.5$ power-law photoionization models, which reasonably reproduce the optical line ratios of low redshift radio galaxies, cannot explain the observed UV line ratios of high- z radio galaxies. Instead a harder ionizing continuum of $\alpha = -1.0$ gives a good fit to their data, with the points falling in the region between predictions for front and rear viewed clouds.

VTC97 also compared their data to the same DS96 shock models as described in this paper. In their diagrams (Figure 3 in VTC97) the emission line ratios for the precursor gas of the shock models were plotted separately, rather than summing the shock and precursor spectra to form a shock+precursor grid. As described in section 3.1, plotting the precursor line ratios separately is inappropriate because the precursor gas is not spatially resolved from the shock gas in these distant galaxies. We have therefore recomputed these same diagrams in Figure 4, with the properly combined shock+precursor grid, and the shock-only grid. We plot the data points from VTC97. Note that this data set does not include the rest wavelength optical lines, or the C II] $\lambda 2326$ line because these lines are redshifted outside the spectral coverage. As such we cannot use the more sensitive diagnostics presented in Figure 2. For completeness we compare these points to our photoionization models, the $A_{M/I}$ sequences (for a wider range of $A_{M/I}$ than used by VTC97), and our observations of nearby AGN. We find that our simple photoionization models behave in a similar way on these diagrams to the photoionization models presented in VTC97.

In Figure 4 we find that the shock-only models cannot account for the observed high- z galaxy

line ratios. The shock+precursor models overlap approximately one quarter of the observed points however the grids exhibit somewhat complicated behaviour on these diagrams, having a number of regions with multiple solutions for the line ratios. The photoionization models appear to explain the trends in the data set by varying the ionization parameter. For example in Figures 4e and 4f the points fall along the photoionization models with ionization parameter in the range $10^{-2} < U < 10^{-1.5}$, whereas the shock+precursor model grid overlaps only a subset of the data points. As such, the shock+precursor models are not able to explain the trends in the data, in terms of shock parameters, and we confirm the conclusion of VTC97 that an $\alpha = -1$ power-law photoionization model provides a good fit to the line ratios.

As high redshift galaxies may have abundances that are less than solar, we include an arrow indicating the shift of the model grids due to a depletion of 0.5 dex in the Carbon abundance. The effect of resonance scattering of C IV $\lambda 1549$ is considered in detail by Villar-Martin, Binette, & Fosbury (1996) and a decreased abundance of Carbon (~ 0.2 dex), could explain the offset of the high- z AGN relative to the nearby AGN.

Comparing our data set of nearby AGN to the models on these diagrams, we find that the NGC 1068 point falls on the shock+precursor grids with shock parameters consistent with those inferred by Figures 2a, 2b and 2d. The other Seyferts, NGC 5643 and NGC 5728 also fall close to the shock+precursor models in the same sense as the previous diagrams, but the models are not as well separated on these diagrams and the Seyferts also fall on the the $\alpha = -1$ photoionization grid with ionization parameters in the range $10^{-2.2} < U < 10^{-1.9}$. Similarly the shock-only and photoionization model grids are degenerate in Figure 4, making it difficult to determine the excitation mechanism for LINER-like spectra using these ratios alone, and we emphasize again that the more sensitive diagnostics in Figure 3 allow us to discriminate between pure shocks and photoionization.

4. CONCLUSIONS

In this paper we have presented UV and UV-optical diagnostic diagrams that are able to discriminate between shock and photoionization predictions for the line ratios in the narrow emission line regions in AGN. These diagnostics rely on the differences between the model predictions of the high ionization lines for separating shock line ratios from photoionization. In general, the diagrams discussed here show that we can, to a large extent, separate photoionization from shocks with precursors if the shock velocity is less than 400 km s^{-1} . Above 400 km s^{-1} the shock+precursor grids overlap with the photoionization models. The most useful diagnostics utilize the C II] $\lambda 2326$ /C III] $\lambda 1909$, C IV $\lambda 1549$ /C III] $\lambda 1909$ ratio pair, and also the near UV [Ne V] $\lambda 3426$ /[Ne III] $\lambda 3869$ ratio provides good diagnostic that can be easily measured with ground based instruments. These UV diagnostics are expected to form a useful observational tool for comparison with UV spectra obtained with the FOS and particularly for spatially mapped UV spectra that will be obtained with STIS. We also have demonstrated that the FUV lines C III $\lambda 977$ and N III $\lambda 991$ are sensitive

temperature diagnostics which can discriminate between the models.

The results in this paper are based on observations made with the NASA/ESA Hubble Space Telescope, obtained at the Space Telescope Science Institute, which is operated by the Association of Universities for Research in Astronomy, Inc., under NASA contract NAS5-26555. MD thanks the Australian Dept. of Industry, Science and Tourism (DIST) for support under a International Science and Technology (IS&T) major grant, which facilitated publication costs and travel. MA acknowledges the support of a Studentship at the Johns Hopkins University (1995-6) through grants GO-4371.01, GO-5426.01 and GO-5926.02 and travel support from the DIST IS&T major grant. ZT was supported in part through NASA grants NAG5-1630 and NAGW-4443 to the Johns Hopkins University.

REFERENCES

- Aldrovandi, S. M. V., & Contini, M. 1984, *A&A*, 140, 368
- Antonucci, R. R. J., & Miller, J. S. 1985, *ApJ*, 297, 621
- Baldwin, J. A., Phillips, M. M., & Terlevich, R., 1981, *PASP*, 93, 5 (BPT)
- Bicknell, G. V. & Begelman, M. C. 1996, *ApJ*, 467, 597
- Bicknell, G. V., Dopita, M. A., & O’Dea, C. P. 1997, *ApJ*, (in press)
- Binette, L., Dopita, M. A., & Tuohy, I. R. 1984, *ApJ*, 297, 476
- Binette, L., Courvoisier, T. J.-L., & Robinson, A. 1988, *A&A*, 190 29
- Binette, L., Wilson, A. S., & Storchi-Bergmann, T. 1996, *A&A*, 312, 365 (BWS96)
- Blum, R. D., & Pradhan, A. K. 1992, *ApJS*, 80, 425
- Capetti, A., Axon, D. J., Macchetto, F., Sparkes, W. B., & Boksenberg, A. 1996, *ApJ*, 469, 554
- Capetti, A., Axon, D. J., Kukula, M., Macchetto, F., Pedlar, A., Sparkes, W. B., & Boksenberg, A. 1995, *ApJ*, 454, L85
- Cardelli, J.A., Clayton, G.C., & Mathis, J.S., 1989, *ApJ*, 345, 245
- Colbert, E. J. M., Baum, S. A., Gallimore, J. F., O’Dea, C. P., Lehnert, M. D., Tsvetanov, Z. I., Mulchaey, J. S., & Caganoff, S. 1996, *ApJS*, 105, 75
- Diaz, A. I., Pagel, B. E., & Wilson, I. R. G. 1985, *MNRAS*, 212, 737
- Dopita, M. A., & Sutherland, R. S. 1995, *ApJ*, 455, 468 (DS95)
- Dopita, M. A., & Sutherland, R. S. 1996, *ApJS*, 102, 161 (DS96)
- Dopita, M. A. 1997, *NGC 1068 Workshop Proceedings*, *Ap & SS*, Summer 1997.
- Dopita, M. A., Koratkar, A. P., Allen, M. G., Tsvetanov, Z. I., Ford, H. C., Bicknell, G. V., & Sutherland, R. S. 1997, (in press) *ApJ*, vol 490
- Dufton, P. L., Berrington, K. A., Burke, P. G., & Kingston, A. E. 1978, *A&A*, 62, 111
- Elston, R., McCarthy, P. J., Eisenhardt, P. Dickinson, M., Spinrad, H., Januzzi, B. T., & Maloney, P. 1994, *AJ*, 107, 910
- Ferguson, J. W., Ferland, G. J. & Pradhan, A. K. 1995, *ApJ*, 438, L55
- Ferland, G. J., & Osterbrock, D. E. 1986, *ApJ*, 300, 658

- Ho, L. C., Filippenko, A. V., & Sargent, W. L. 1993, *ApJ*, 417, 63
- Ho, L. C., Shields, J. C., & Filippenko, A. V. 1993, *ApJ*, 410, 567
- Kirhakos, S., & Phillips, M. M. 1989, *PASP*, 101, 949
- Kriss, G. A., Davidsen, A. F., Blair, W. P., Ferguson, H. C. & Long, K. S. 1992, *ApJ*, 394, L37
- Leitherer et al., 1996, *PASP*, 108, 996
- McCarthy, P. J., Spinrad, H., van Breugel, W. J. M., Liebert, J., Dickinson, M., Djorgovski, S., & Eisenhardt, P. 1990, *ApJ*, 365, 487
- McCarthy, P. J. 1993, *ARA&A*, 31, 639
- Morganti, R., Robinson, A., Fosbury, R. A. E., di Serego Alighieri, S., Tadhunter, C. N., Malin, D. F. 1991, *MNRAS*, 249, 91
- Morse, J. A., Raymond, J. C., & Wilson, A. S. 1996, *PASP*, 108, 426
- Osterbrock, D. S., Tran, H. D., & Veilleux, S. 1992, *ApJ*, 389, 196
- Pogge, R. W. 1989, *ApJ*, 345, 730
- Robinson, A. Binette, L., Fosbury, R. A. E., & Tadhunter, C. N. 1987, *MNRAS*, 227, 97
- Simpson, C. J., Wilson, A. S., Bower, G. A., Heckman, T. M., Krolik, J. H., & Miley, G. K. 1997, *ApJ*, 474, 121
- Snijders, M. A. J., Netzer, H., & Boksenberg, A. 1986, *MNRAS*, 222, 549
- Spinrad, H., Filippenko, A. V., Wyckoff, S., Wagner, R. M., & Stocke, J. T. 1985, *ApJ*, 299, L7
- Stasinska, G. 1984, *A&AS*, 55, 15
- Storchi-Bergmann, T., Wilson, A. S., Mulchaey, J. S., & Binette, L. 1996, *A&A*, 312, 357
- Sutherland, R. S., Bicknell, G., V., & Dopita, M. A. 1993, *ApJ*, 414, 510
- Sutherland, R. S. & Dopita, M. A. 1993, *ApJS*, 88, 253
- Pedlar, A., Dyson, J. E., & Unger, S. W. 1985, *MNRAS*, 214, 463
- Tadhunter, C. N., Robinson, A., & Morganti, R. 1989, in *Extranuclear Activity in Galaxies*, ed. E. J. A. Meurs & R. A. E. Fosbury (Garching, ESO). p293
- Tadhunter, C. N. & Tsvetanov, Z. I., 1989, *Nature*, 341, 422
- Taylor, D., Dyson, J. E. & Axon, D. J. 1992, *MNRAS*, 228, 121

- Veilleux, S., & Osterbrock, D. E. 1987, *ApJS*, 63, 295
- Viegas, S. M., & Prieto, M. A. 1992, *MNRAS*, 258, 483
- Viegas-Aldrovandi, S. M., & Contini, M. 1989, *ApJ*, 339, 689
- Villar-Martin, M., Binette, L., & Fosbury, R. A. E. 1997, *A&A*, 312, 751
- Villar-Martin, M., Tadhunter, C. N., & Clark, N. E. 1997, *A&A*, in press. (VTC97)
- Wilson, A. S., Braatz, J. A., Heckman, T. M., Krolik, J. H., & Miley, G. K. 1993, *ApJ*, 419, L61
- Wilson, A. S. 1996, in *Emission Lines in Active Galaxies: New Methods and Techniques*, ed. B. M. Peterson, F.-Z. Cheng, and A. S. Wilson, *Astron. Soc. Pac. Conf. Ser. Vol. 113*, 264
- Wilson, A. S., Ward, M. J. & Haniff, C. A. 1988, *ApJ*, 334, 121
- Wilson, A. S., & Tsvetanov Z. I. 1994, *AJ*, 107, 1227
- van Ojik, R. 1995, Ph.D. thesis, Rijksuniversiteit te Leiden

Table 1. Observations

Object	Instrument	λ
NGC 5643	<i>HST</i> FOS	1150 – 2500
	MSSSO 2.3m telescope	3000 – 10000
NGC 5728	<i>HST</i> FOS	1150 – 2500
	MSSSO 2.3m telescope	3000 – 10000
M87	<i>HST</i> FOS ¹	1150 – 6820
NGC 1068	various ²	977 – 9600
	HUT ³	830 – 1860
	IUE ⁴	~1100 – 3300

References. — (1) Dopita et al.; (2) compiled in Dopita; (3) Kriss et al. (1992); (4) Snijders, Netzer, & Boksenberg (1986)

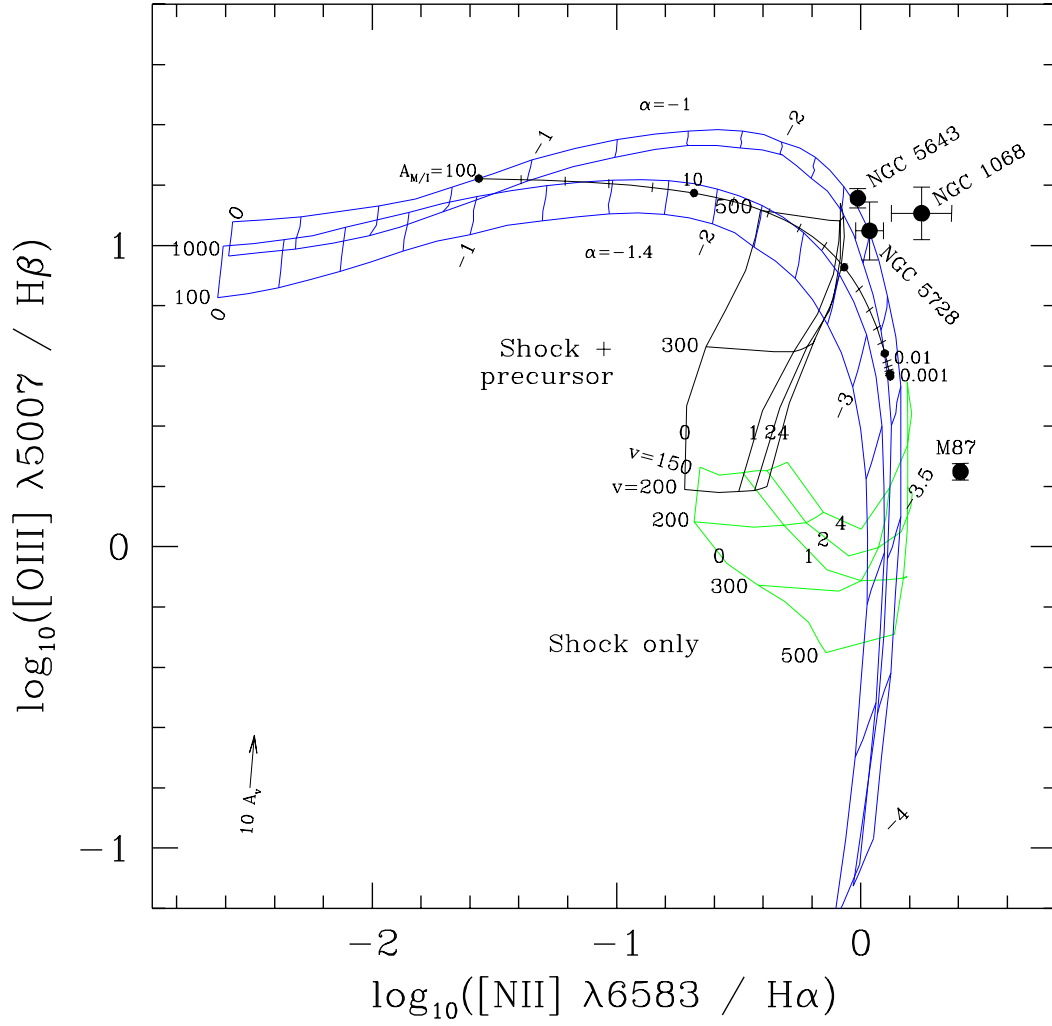


Fig. 1.— Optical diagnostic diagram.

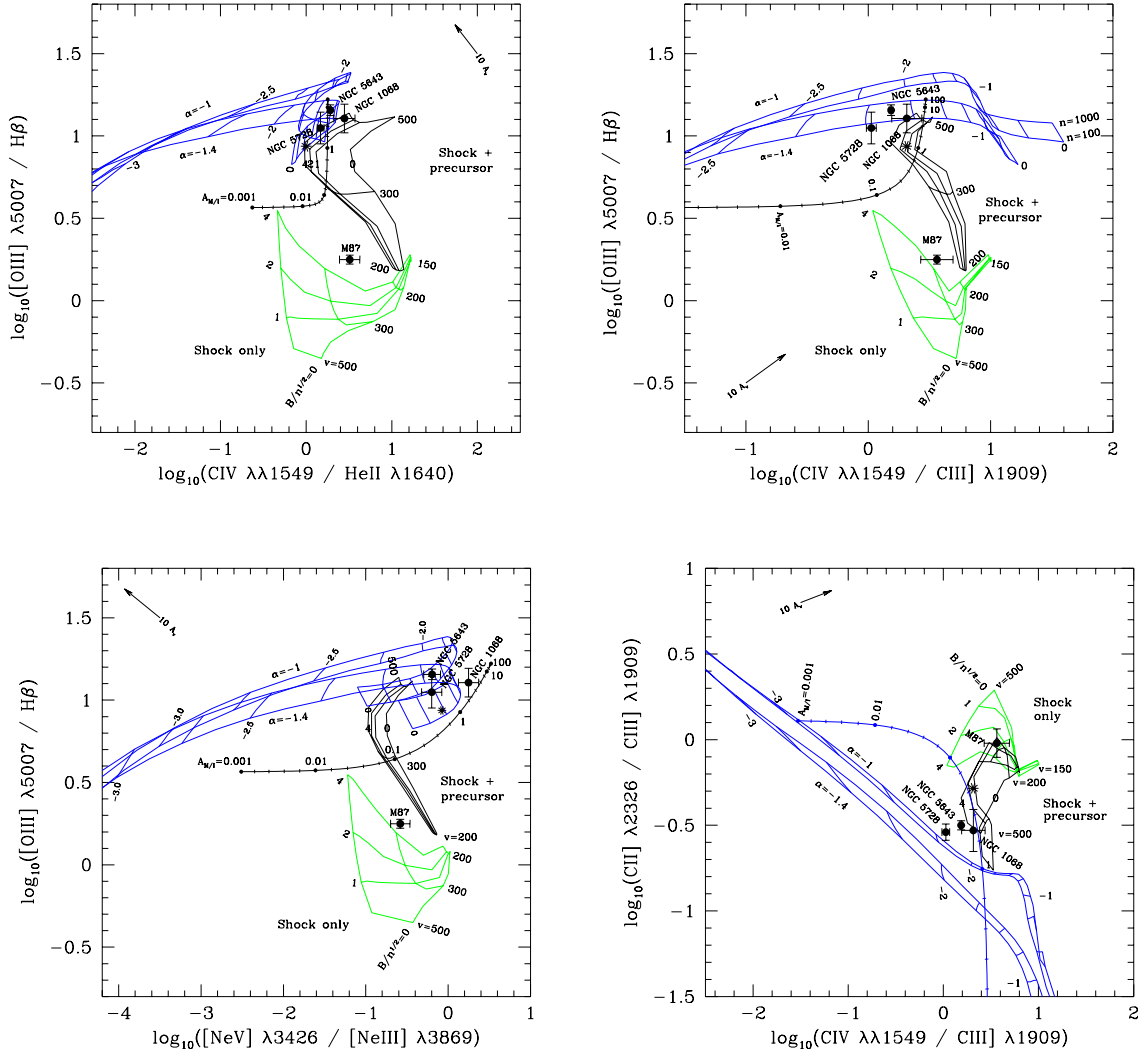


Fig. 2.— UV and UV-optical diagnostic diagrams.

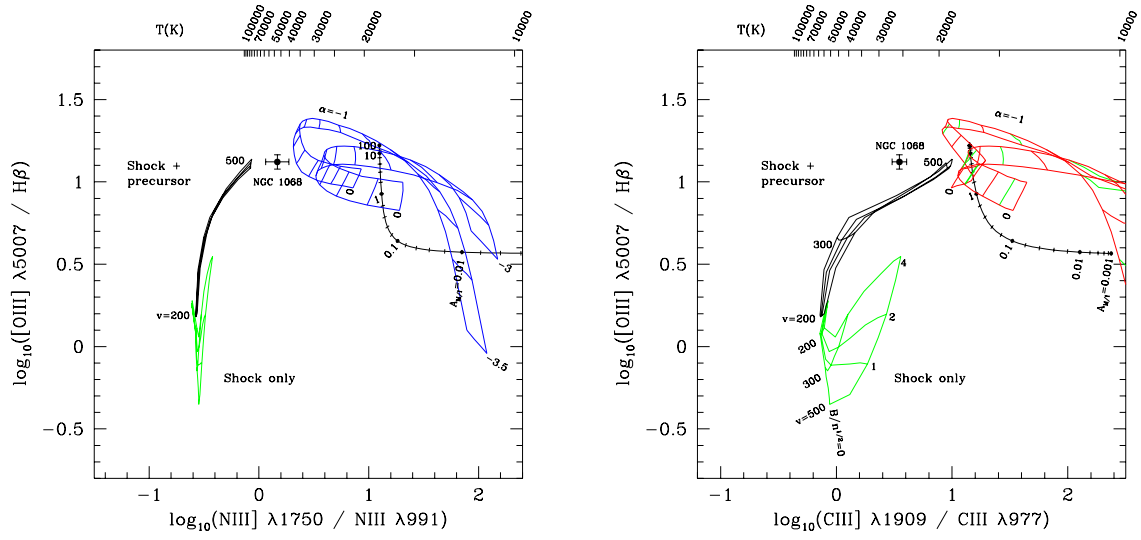


Fig. 3.— Temperature sensitive diagnostic diagrams.

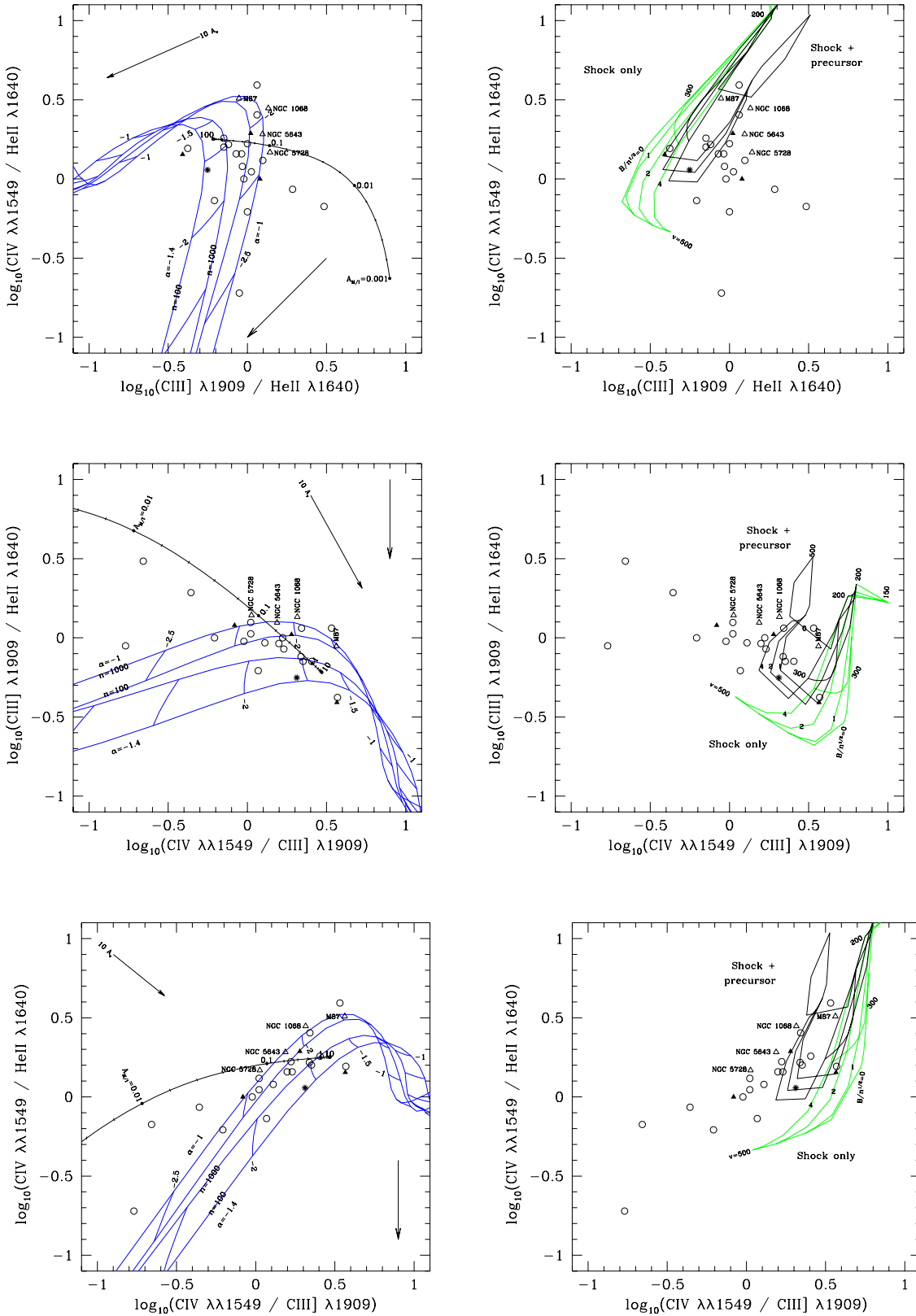


Fig. 4.— UV diagnostic diagrams from Villar-Martín et al. (1997). The open circles are van Ojik’s (1995) HZRG and the solid triangles are other published HZRG line fluxes. The star is the average HZRG of McCarthy (1993)